Nanoscale Horizons

ROYAL SOCIETY OF CHEMISTRY

COMMUNICATION

View Article Online
View Journal | View Issue

Cite this: *Nanoscale Horiz.*, 2025, **10**, 2865

Received 30th May 2025,
Accepted 7th August 2025

DOI: 10.1039/d5nh00375j

rsc.li/nanoscale-horizons

Nanophase separation and interfacial entanglements enable tough hybrid polymer networks

Xunan Hou, †[a] Liang Ma,†[a] Zhihao Zhang,[ab] Zichun Zhu,[a] Hao Wang,[a] Peiyao Yan,[a] Zhuang Wang[a] and Chaobin He *[ac]

Elastomers and hydrogels are essential components in soft robotics and biomedical devices due to their flexible and swollen polymer networks. However, designing soft polymeric materials that reconcile tunable water content and mechanical performance remains a key challenge. Here, we report hybrid polymer networks toughened by nanoscopic arrested phases. The as-prepared, dry elastomeric networks demonstrate a 4- to 25-fold synergistic enhancement in ductility while maintaining high moduli and strength. When fully hydrated, the blend gels display tunable swelling ratio (150–413%), moduli spanning 2 orders of magnitude (6.4–200 MPa), high elongation (230–410%) and toughness (2.5–4.4 kJ m^{-2}). Such properties are rarely accessible in conventional gels. Morphological investigation reveals distinct reinforcing nanophases of hydrophobic chains, while viscoelastic measurement shows dense entanglements. This platform bypasses traditional solution-based methods, offering a scalable route to tough, functional hydrogels. Our findings establish a blueprint for soft, multiphase materials for soft actuators or biomedical implants.

New concepts

We introduce a solvent-free strategy to create hydrogels with tunable water content and exceptional mechanical robustness through nanoscale arrested phase separation and interfacial entanglements. Unlike conventional hydrogels synthesized in solution—where solvents dilute entanglements and limit mechanical performance—our method utilizes melt-processed blends of hydrophilic (PEG) and hydrophobic (amorphous PLA) polymers. Upon hydration, thermodynamically driven phase separation is arrested at the nanoscale (<100 nm) by dense entanglements at the domain interfaces. This yields hydrogels that defy the classic stiffness–toughness trade-off, achieving unprecedented combinations of swelling (up to 413%), modulus (6.4–215 MPa), and toughness (up to 4.4 kJ m^{-2})—properties inaccessible to existing single-network, double-network, or entangled hydrogels. The platform bypasses solvent-dependent processing, enabling scalable fabrication of amphibious materials that function as ductile elastomers when dry and as ultra-tough hydrogels when swollen. This entanglement-driven nanophase design establishes a universal blueprint for next-generation soft materials in soft robotics, biointerfaces, and tissue engineering.

Introduction

Hydrogels and elastomers play a central role in a wide range of biomedical and engineering applications, including tissue implants and soft robotics.[1–4] These materials are required to combine water swelling and flexibility with sufficient mechanical integrity to withstand deformation. However, a persistent challenge is the inherent trade-off between stiffness and toughness in polymer networks.[5–7] Soft, single-network hydrogels are often highly elastic but mechanically weak, whereas stiffening the matrix typically reduces extensibility and leads to brittleness.[8,9] This modulus–toughness conflict remains a fundamental bottleneck for the development of durable soft materials.

To address this limitation, a number of hydrogel toughening strategies have been proposed. One of the most established approaches is the double network (DN) design, which incorporates a brittle sacrificial network within a stretchable secondary matrix.[10–13] While DN gels achieve high toughness through hydrophilic interactions and physical entrapments, the sparse entanglements and short secondary network lead to high hysteresis. More recently, homogeneous entangled networks (HENs) have emerged as a promising class of soft materials, offering high elasticity and moderate toughness.[13–15] Nevertheless, densely entangled chains are attainable only at high monomer concentrations or ultrahigh molecular weights,[15,16] which poses challenges in processing and reproducibility. HENs are constrained by their single-phase architecture, which limits the extent of network reinforcement without compromising water content or

[a] *Department of Materials Science and Engineering, National University of Singapore, 9 Engineering Drive 1, 117575, Singapore. E-mail: msehc@nus.edu.sg*
[b] *State Key Laboratory of Advanced Fiber Materials, College of Materials Science and Engineering, Donghua University, Shanghai 201620, China*
[c] *Institute of Materials Research and Engineering, Agency for Science, Technology and Research (A*STAR), 2 Fusionopolis Way, Innovis, 138634, Singapore*
† These authors contributed equally to this paper.

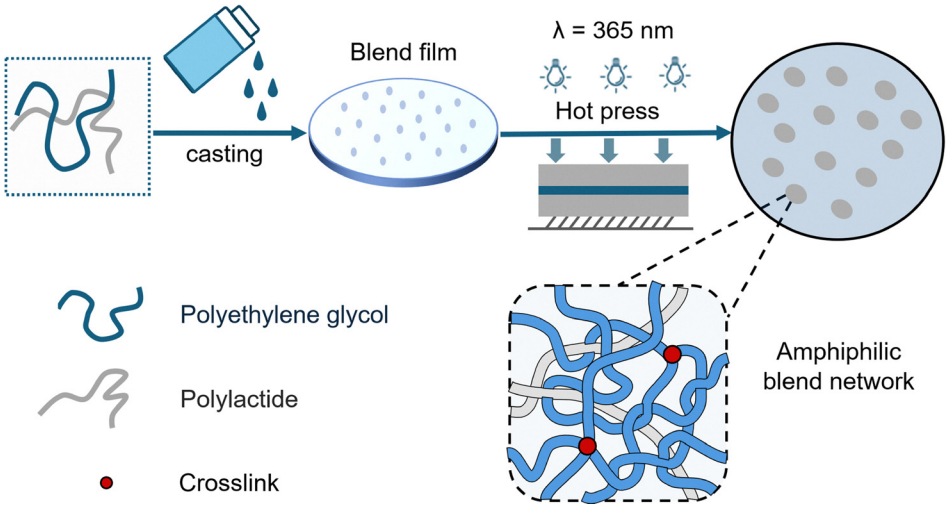

Fig. 1 Preparation scheme of a nanophase separated blend network with interfacial entanglements.

transparency.[17,18] An alternative path has emerged through heterogeneous hydrogel designs, including arrested phase-separated systems, where network domains are formed by localized crystallization or incompatibility-driven segregation.[19–21] While these strategies demonstrate remarkable improvements in modulus and fracture toughness, their fabrication still relies on solution-based polymerization,[3,22] where the presence of solvents dilutes entanglements and complicates phase stabilization.[4,17] In single networks, densely entangled chains are attainable only at ultra-high monomer concentrations or molecular weights,[15,16] which poses challenges in processing and reproducibility. Recent works reveal that entropic miscibility facilitates entanglements and toughness in polymer blends.[23,24] Extending this principle, we hypothesize that miscible blends could facilitate entanglements in hydrogels.[25]

In this study, we develop a nanophase blend system to toughen hydrogels based on polyethylene glycol (PEG) and polylactide (PLA). Long-chain amorphous PLA induces highly entangled, arrested phase-separated structures that dramatically enhance mechanical performance while allowing tunable swelling behavior. The crosslinking involves simple thermal casting without a solvent, yielding ductile and tough elastomers with controlled nanophase separation. In the dry state, they behave like tough elastomers with high strength and ductility. When swollen into gels, the materials are highly elastic and tough. These findings establish a scalable route for designing tough polymer networks, offering a promising platform for next-generation smart soft materials.

Results and discussion

Design of blend networks

We propose a hydrogel design utilizing melt entanglements of network polymer blends. As shown in Fig. 1, PLA and PEG were dissolved at high concentrations and casted to remove all solvents. The blend film was then subjected to hot pressing and UV curing into an elastomer. Since PLA is hydrophobic but thermodynamically miscible with PEG, we envision swelling to induce nanodomain separation, while mutual miscibility could form dense entanglements at the interface.[26] Based on this design, we hypothesize that a long chain PLA could offer maximum entanglements in the PEG network without the hindrance of crystalline domains. To validate this hypothesis, we choose an amorphous, long-chain poly(D,L-lactide) random copolymer with 10% D-lactide content, denoted as aPLA. The resultant PEG/aPLA blends are denoted as XXaPLA, where XX denotes the mass percentage of aPLA and ranges from 0 to 100 (Fig. 2).

Morphology and mechanics of arrested nanophase blends

We compare the morphology and mechanical behavior of crosslinked PEG/aPLA blends under ambient and swollen conditions. The as-prepared dry blend is macroscopically homogeneous and translucent above the PEG melting point. SEM shows a relatively smooth surface with occasional defects arising from melt processing. Upon swelling, numerous micropores emerge on the surface, constituted by nanopores, suggesting the presence of aPLA-rich and PEG-rich domains. The 2 states are reversible, resembling an arrested phase separation. Notably, the resulting polymer material is amphibious and demonstrates outstanding mechanical properties in both dry and wet states. Uniaxial tensile tests on PEG/aPLA dry blends demonstrate thermoplastic-like behaviors with an elongation of 400–650%, exceeding that of aPLA and even crosslinked PEG, while maintaining high strengths of 8–15 MPa. When equilibrated in water, the gels outperform neat PEG hydrogels by 2 orders of magnitude in moduli (6.4–215 MPa), strength (2.5–11 MPa) and elongation (230–410%, Table 1). Understanding of the underlying mechanism requires further structural comparisons of different chain lengths and molecular weights.

Structural origin of toughening

To understand the effect of chain architecture on network morphology, we compare the results with crystallizable PLA

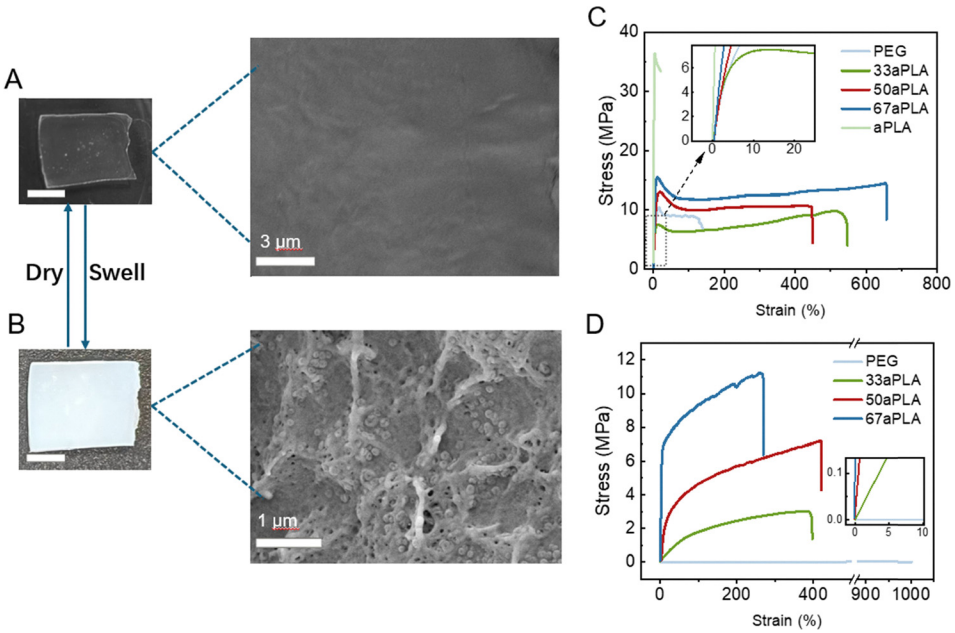

Fig. 2 Digital images and SEM images of the 33aPLA blend: (A) crosslinked dry blend and (B) swollen hydrogel; PLA rich domains are shown in red. Stress–strain curves of the PEG/aPLA blend at different aPLA contents: (C) dry blend and (D) swollen hydrogels.

(cPLA) and short-chain PLA (sPLA). All blends were freeze-dried and visualized by SEM. 33cPLA exhibited micron phase separation (1–2 μm) connected by submicron pores, indicating crystalline domains. 33aPLA exhibits ultrafine nanopores well below 100 nm. Close scrutiny shows embedded aPLA nanoparticles with typical diameters of ~200 nm. Meanwhile, sPLA displays much larger and uneven pores at 5–30 μm, suggesting macroscopic phase separation and a lack of entanglements. The equilibrium swelling ratio (SR) of blend hydrogels further corroborates this point. 33cPLA and 33aPLA blends exhibited comparable SR values well below the mixture rule (M-R) prediction. In contrast, the 33sPLA blend demonstrated markedly higher swelling up to 10 times, indicative of reduced polymer chain entanglement. This trend implies that entanglements with long chains play a critical role in anti-swelling, which preserves hydrogel network cohesion and dimensional stability.

Rheological characterization revealed further distinctions. Both 33aPLA and 33sPLA blends displayed elevated storage (G') and loss (G'') moduli, whereas 33cPLA exhibited a pronounced decrease in viscoelastic response. This reduction is attributed to the melting or softening of crystalline domains under the high-temperature testing conditions (150–160 °C), which may disrupt the network structure. Notably, 33aPLA consistently maintained a larger storage modulus at higher frequencies, while 33sPLA only approached similar values at low frequencies. This suggests the strengthening effects of entanglements in long-chain aPLA. These results underscore the different origins of storage moduli: 33aPLA imparts stiffness *via* extensive entanglement and phase arrest, while 33cPLA contributes through transient crystalline reinforcement that may be thermally labile.

Mechanical testing of the densified hydrogels at 33 wt% PLA further highlights these differences. The 33sPLA blend remained soft and compliant, with a low modulus of ~20 kPa, reflecting its limited network integrity and poor load transfer. 33cPLA achieved moderate stiffness (~5 MPa) but failed prematurely, indicating brittle fracture and a lack of energy dissipation mechanisms. In stark contrast, 33aPLA blends displayed superior performance, achieving a modulus of 6.3 MPa, a tensile strength of 3 MPa, and elongation at break exceeding 400%. These results point to a unique toughening mechanism arising from the melt-densified amorphous domains, which promote topological entanglement without the brittleness typically associated with crystallinity. Notably, this enhanced ductility and toughness persist even at high PLA

Table 1 Mechanical properties of PEG/aPLA blend hydrogels

aPLA%	Modulus (MPa)	Strength (MPa)	Elongation (%)	Fracture energy (MJ m^{-3})	Toughness (kJ m^{-2})
0	0.02 ± 0.003	0.025 ± 0.002	980.42 ± 39.95	0.12 ± 0.015	0.008
33	6.38 ± 2.45	2.91 ± 0.54	398.19 ± 31.64	8.65 ± 3.78	2.257
50	35.07 ± 5.97	6.27 ± 0.68	410.73 ± 27.49	15.61 ± 5.14	9.070
67	213.01 ± 20.48	10.50 ± 0.67	286.25 ± 21.28	20.17 ± 4.51	6.132
100	1227 ± 213	36.81 ± 1.52	26.56 ± 3.81	6.78 ± 0.89	3.608

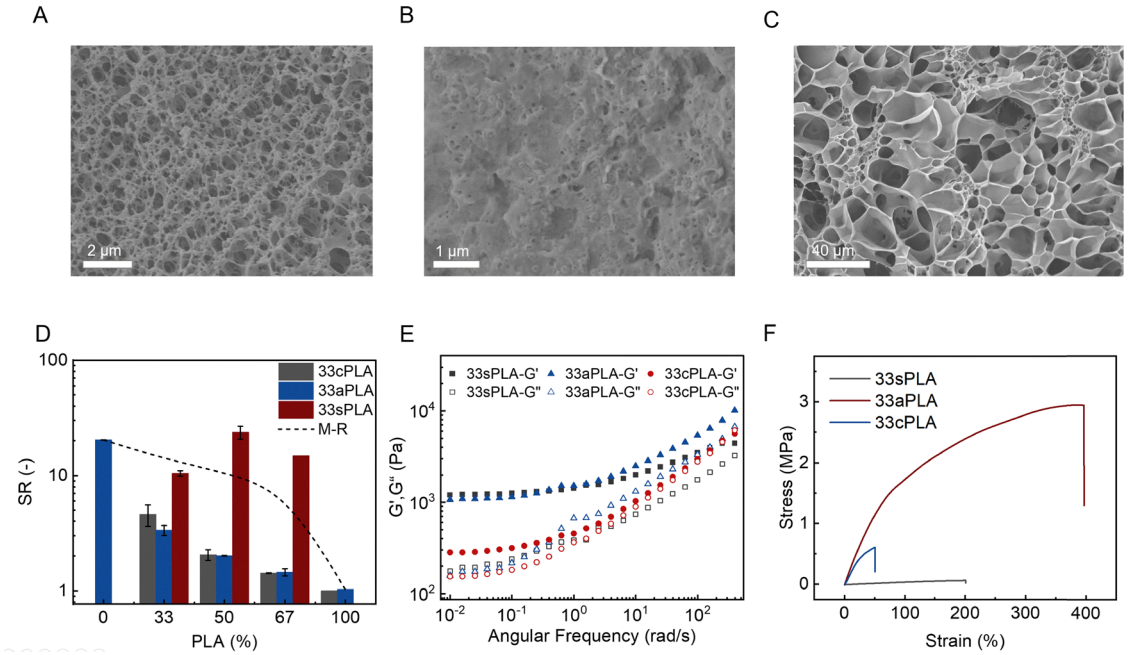

Fig. 3 Morphology, entanglements and mechanics in different blend networks. SEM images of freeze-dried blend networks: (A) 33cPLA; (B) 33aPLA; and (C) 33sPLA. (D) Swelling ratio of PEG/PLA blend hydrogels; M-R denotes mixture rule predictions. (E) Storage (G') and loss (G'') moduli of dry blend melts with different types of PLA. (F) Stress–strain curves of hydrated PEG/PLA blends.

loadings (33 wt%), a composition range often associated with embrittlement in traditional PLA blends.

Crystallinity and molecular weight effects

To further confirm the molecular origins of effective toughening, we performed chemical and structural characterizations of the dried gel films (Fig. 4). FTIR spectra revealed characteristic carbonyl absorptions near 1750 cm^{-1} for all PLA-containing samples (Fig. 4A). The 33cPLA blend exhibited a more intense and broadened absorption with a clear shoulder, suggesting the presence of ordered crystalline regions. This was corroborated by WAXD measurements, where the 33cPLA blend displayed a distinct diffraction peak at $2\theta \approx 17^{\circ}$, corresponding to (200/210) planes in PLA α-phase crystallites (Fig. 4B).[27] In contrast, 33aPLA showed only a minor, broadened feature, and 33sPLA was amorphous without discernible peaks. Meanwhile, the PEG diffraction peaks of (120) and (032) planes are nearly identical in all samples, suggesting minimal disruption to its primary crystallization. Differential scanning calorimetry (DSC) confirmed these findings: only the 33cPLA blend exhibited a melting endotherm associated with crystalline PLA, while 33aPLA and 33sPLA remained amorphous (Fig. S1). After solvent etching, the swelling ratio (SR) follows the sequence: cPLA < aPLA < sPLA (Fig. 4C). To quantify entanglement effects on swelling, we define a dimensionless swelling limiting factor (SLF), defined by the swelling ratio in etched samples divided by that in neat samples as follows: $SLF = SR_{etch}/SR_{neat}$. 33aPLA demonstrates the highest SLF value, suggesting denser entanglements within the network. 33cPLA has a lower SLF due to potential hindrance by crystalline domains, while 33SPLA shows the lowest SLF, as its molecular weight M_w lies below the entanglement molecular weight $M_{e,PLA} \approx 15$ kDa. SEM images show smaller and more uniform pores in 33aPLA compared to the other two blends (Fig. 4D–F). It also exhibits a distinct border between pores, while the others show bulkier PEG phases separating the pores. These traits point to a more homogeneous mixing and uniform network in aPLA blends, consistent with previous data (Fig. 3A–C). We further performed a statistical analysis of the pore sizes in the etched hydrogels (Fig. S4). The etched cPLA33 and sPLA33 samples exhibited a broad and irregular pore size distribution ranging from 1 to 20 μm, indicating non-uniform pore formation and suggesting heterogeneous dispersion of PLA domains, which may introduce more structural defects. In contrast, the etched aPLA33 sample displayed a narrower and more concentrated pore size distribution, primarily between 7 and 11 μm, implying a more homogeneous dispersion of PEO and PLA phases. These results are consistent with the previous conclusions and further support the superior structural uniformity of aPLA33 (Fig. 5) (Table 2).

Table 2 Range of mechanical properties in melt-crosslinked gels with conventional and other reported tough gels

Material	Modulus (MPa)	Toughness (kJ m^{-2})	Ref.
PAAm gels	0.01–0.09	0.01–0.05	20
HESN gel	0.15–0.4	0.05–0.8	13, 28
DN gel	0.09–1.5	0.08–0.6	13, 29
Annealed PVA gel	1.0–1.8	0.6–2	21
Mineralized gel	55–150	0.4–1.2	30
PDMS rubber	20–250	1.5–3.6	28
NPS gel	6.4–200	2.5–4.3	This work

Synergetic toughening in NPS blends and hydrogels

The robustness and durability of polymer networks are characterized by their fracture energy E_f and notched toughness Γ.

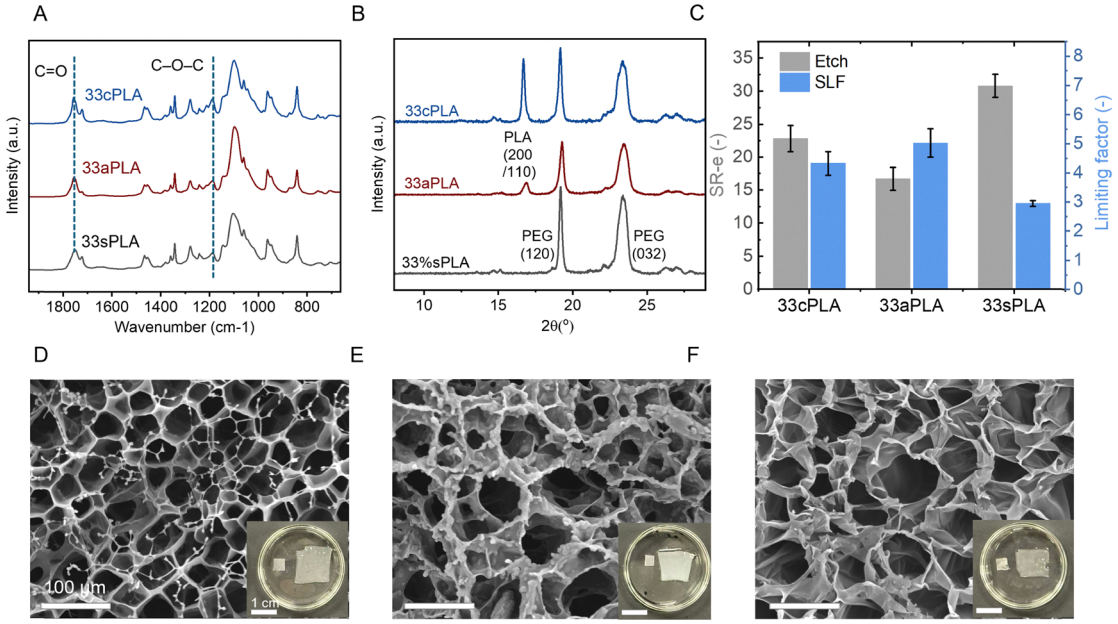

Fig. 4 Structural origin of entangled nanoscale networks. (A) FTIR spectra; (B) wide angle X-ray diffraction; (C) swelling ratio (SR) after etching and swelling limitation factor at 33% PLA loading. SEM images of solvent etched samples: (D) 33aPLA; (E) 33cPLA; and (F) 33sPLA.

Neat PEG is brittle (E_f = 0.1 MJ m^{-3}) and notch sensitive (Table 1, Γ = 30 J m^{-2}). Incorporating 33% of PLA drastically enhances E_f (0.8 MJ m^{-3}) and Γ (2.5–4.3 kJ m^{-2}) by over 2 orders, suggesting the effective reinforcement by entangled nanodomains. The performance of NPS gels is benchmarked against state-of-the-art tough hydrogels. Both moduli and toughness surpass those of conventional gels such as PAAm by 2 orders of magnitude. The combination of properties also exceeds those of common tough hydrogels crosslinked in solution, such as HESN, DN, and mineralized gels, on par with commercial elastomeric materials such as rubbers. Since this method relies on fundamental thermodynamics and solvent-

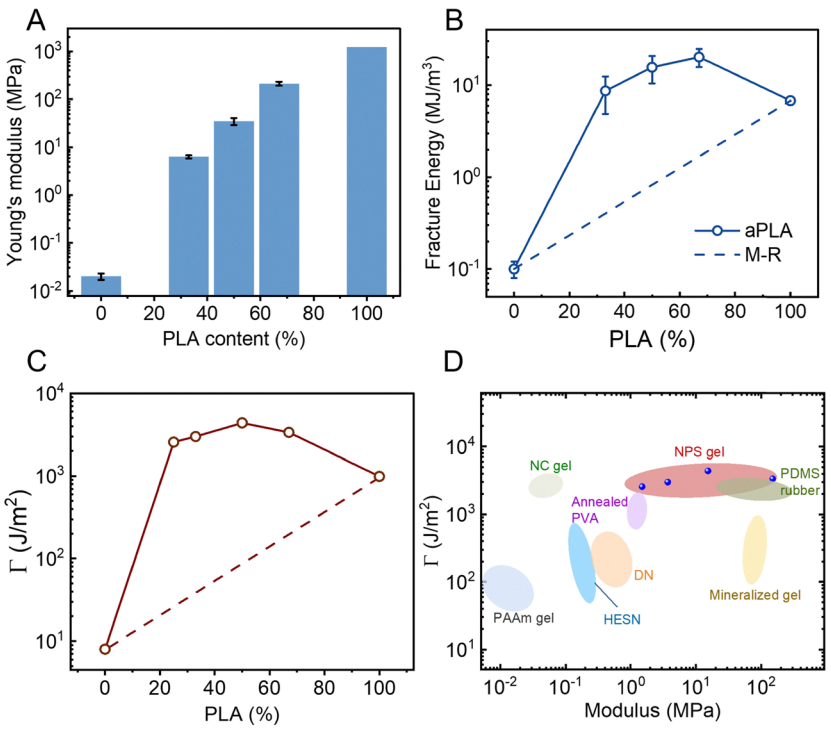

Fig. 5 Mechanical durability. Performance of NPS hydrogels as a function of PLA content: (A) Young's moduli; (B) fracture energy; and (C) notched toughness Γ. (D) Ashby plot of modulus–toughness relations in NPS gels compared with other tough hydrogels and elastomers.

induced nanophases, it could be applied to multiple systems beyond PEG/PLA blends.

Conclusions

We have demonstrated a broadly applicable strategy for creating nanophase-separated PEG/PLA networks that combine tunable water content with exceptional mechanical robustness. By rationally choosing PLA chain length and crystallinity, interfacial entanglements arrest phase separation at the nanoscale, yielding dry elastomers with elongations exceeding 600% and fully swollen hydrogels that combine 6–215 MPa stiffness with toughness values as high as 4.3 kJ m^{-2} and elongations of 230–410%. This entanglement-driven mechanism bypasses the irreversible damage and processing complexity of double networks or freeze-cast gels, offering a scalable, high-throughput route to durable soft materials. Moving forward, integrating functional nanofillers such as piezo- or ferroelectric ceramics into this arrested matrix could enable multifunctional platforms for soft robotics, biointerfaces, and implantable devices, where programmable mechanics and responsive properties are equally critical.

Materials and methods

Materials

All polymers used in this study were commercially available. Poly(ethylene oxide) (PEO, M_w = 35 000 g mol^{-1}) and poly(D,L-lactide) (PDLLA, M_n = 10 000) were obtained from Sigma-Aldrich Company. cPLA (cPLA, Ingeo 3051D, M_w = 160 000 g mol^{-1}, M_w/M_n = 1.6) and aPLA (Ingeo 4060D, 10% D-lactide, M_w = 170 000 g mol^{-1}, M_w/M_n = 1.7) were purchased from Natureworks LLC, USA. The photoinitiator benzophenone (BP) was purchased from TCI and used as received.

Preparation of polymer blends and NPS gels

The polymer blend was prepared by a solution casting method. Taking the 33aPLA sample as a representative example, the procedure consisted of four main steps:

First, 2 g of PEO was dissolved in 10 mL of acetone under stirring at 60 °C until a completely clear solution was obtained. Then, 1 g of DLLA was added to the solution and stirred continuously until it was fully dissolved, forming a transparent homogeneous solution. Subsequently, BP was added at 2 wt% relative to the mass of PEO, and the mixture was stirred thoroughly.

The resulting solution was then uniformly cast onto a glass Petri dish and placed on a heating plate to allow solvent evaporation. After complete drying, a slightly whitish polymer bulk was obtained. To prepare polymer films, a small amount of the polymer bulk was placed in a mold and hot-pressed at 100 °C under 0.5 T pressure for 90 seconds. The mold was then removed and immediately transferred to a UV curing chamber. The sample was irradiated on both sides for 2 × 2 min. The cured polymer initially appeared transparent but turned milky white upon cooling. After complete cooling, the mold was removed, yielding the 33aPLA polymer film. Other compositions were prepared following the same procedure. Finally, the obtained films were immersed in water, where they swelled significantly and became opaque white as water uptake reached equilibrium. The final materials were water-rich polymer composites with hydrogel-like characteristics.

Swelling and solvent etching

The swelling ratio and water content of the hydrogels was determined by assessing their dry and wet mass in various cycles. The as-prepared MCN sample was weighed immediately and immersed in DI water for swelling until the mass equilibrates to obtain its wet mass m_{wet}. Excess surface water was carefully removed using Kimwipes. To verify the swelling, the swollen hydrogels were then dried in a vacuum oven at 60 °C to obtain the dry mass. The wet weight m_w and dry weight m_{dry} were measured using a microbalance. The swelling ratio was defined as SR = m_{wet}/m_{dry}, and the equilibrium water content was calculated as EWC = $(1 - 1/SR) \times 100\%$. At 50 °C, anhydrous dichloromethane was used to selectively etch the dry sample with $m_0 \approx 1$ g for one minute, then it was soaked in acetone solution for one minute to remove dichloromethane, and finally rinsed with deionized water and weighed to obtain its mass m. Then the sample was rehydrated in pure water to produce an etched hydrogel.

Characterization of NPS gels

Scanning electron microscopy (SEM). The morphology of swollen and etched hydrogels was examined using a field-emission scanning electron microscope (Zeiss Supra 40 FE-SEM) operating at a voltage of 5 kV and having an aperture size of 30 μm. The hydrogel samples were immersed in liquid nitrogen for 5 min, freeze-dried overnight and sputter-coated with a ~8 nm thick gold layer. The etched samples were repeatedly washed with water before freezing.

Mechanical properties. To measure the ultimate properties, uniaxial tensile tests of hydrogels were conducted using a double-column universal tester (Instron 5569, USA) equipped with a 100 N load cell. Fully swollen hydrogels were cut into rectangular specimens with dimensions of 60 mm × 10 mm × 0.60 mm, with an initial gauge length H of ~10 mm. Unnotched specimens were subjected to monotonic stretching until failure at a strain rate of 1 min^{-1}. The elastic energy function $W(\varepsilon)$ was obtained by integrating the area under the stress–strain (σ–ε) curve. To evaluate the fracture toughness Γ, a sharp blade was used to introduce a notch at the long side of the sample, and the specimen was stretched to failure, measuring the maximum strain ε_m. The toughness was defined by $W(\varepsilon_m)H$.

Wide-angle X-ray diffraction (WAXD). The crystallization characteristics of hydrogels were measured using a Bruker GADDS X-ray diffractometer (D8 Advance) at 40 mA and 40 kV with Cu Kα radiation (λ = 1.5418 Å). The scanning range was 2θ = 10–40° with a total exposure time of 300 s. The samples were freeze-dried before each measurement and mounted onto a plastic sample holder. Background subtraction and

smoothing were conducted using the instrumental software. The final data were normalized by sample thickness.

Differential scanning calorimetry (DSC). The thermal properties of melt-crosslinked networks were measured using a PerkinElmer DSC6000. The freeze-dried samples were cut into pieces of ~2 mm size using a surgical scalpel (Swann-Morton, USA). ~7 mg of sample pellets were sealed into a robotic pan and subjected to DSC scan: cooling to −30 °C and heating to 140 °C for 2 cycles. The heating rate was 10 °C min^{-1}. The glass transition temperature (T_g) was obtained from the inflection point of step change. The crystallinity X_c in the samples was obtained by

$$X_c = \frac{\Delta H_m}{w\Delta H_c} \quad (1)$$

where ΔH_m and ΔH_{cc} are the enthalpies of melting and w is the weight fraction of PEG in the blend. Note that for all blends at φ = 0.50, no cold crystallization is detected and ΔH_c = 196.8 J g^{-1} is taken as the crystallization enthalpy of pure PEG 35000. Results are shown in Table S3.

Rheological properties. The storage moduli G' and loss moduli G'' of dry blends and swollen hydrogels are measured using an MCR302 rotational rheometer (Anton Paar, Austria) and a parallel plate setup. For melt and solution cured blends, the hot-pressed samples were fully dried in a vacuum oven followed by curing in an UV oven at 300 mW cm^{-2} and placed onto the bottom plate at 160 ± 0.5 °C. For G' and G'', the normal force was set to ~1 N, and the angular frequency was varied from 0.1 to 200 rad s^{-1}.

Fracture toughness testing. The fracture toughness (Γ) of nanocomposites and pristine polymers was evaluated *via* single-edge crack tests. Rectangular specimens (15 mm wide × 60 mm long) with a 4-mm edge crack were tensile-loaded at a 10 mm gauge length. Stress (σ) was calculated as the applied force (F) divided by the uncut cross-sectional area. The energy release rate (G) was determined using the relation: $G = \pi\sigma^2 a/E[1.122 - 0.231(a/b) + 10.55(a/b)^2 - 21.71(a/b)^3 + 30.382(a/b)^4]$, where a is the crack length, b is the sample width, and E is the elastic modulus. The critical stress at fracture (σ_c) was used to calculate the material's toughness (Γ).[31]

Conflicts of interest

There are no conflicts to declare.

Data availability

The data supporting this article have been included as part of the SI. Supplementary information available: Supporting Table S1, Fig. S1–S5. See DOI: https://doi.org/10.1039/d5nh00375j

References

1 C. Yang and Z. Suo, *Nat. Rev. Mater.*, 2018, **3**, 125–142.
2 X. Yang, S. Li, Y. Ren, L. Qiang, Y. Liu, J. Wang and K. Dai, *Composites, Part B*, 2022, **237**, 109863.
3 Y. Lv, C. Li, Z. Yang, M. Gan, Y. Wang, M. Lu, X. Zhang and L. Min, *Adv. Sci.*, 2024, **11**, DOI: 10.1002/advs.202410446.
4 Y. Wang, R. Shu and X. Zhang, *Angew. Chem., Int. Ed.*, 2023, **62**, e202303446.
5 G. J. Lake and A. G. Thomas, *Proc. R Soc. Lond. A Math. Phys. Sci.*, 1967, **300**, 108–119.
6 J. Cui, M. A. Lackey, A. E. Madkour, E. M. Saffer, D. M. Griffin, S. R. Bhatia, A. J. Crosby and G. N. Tew, *Biomacromolecules*, 2012, **13**, 584–588.
7 T. L. Sun, T. Kurokawa, S. Kuroda, A. Bin Ihsan, T. Akasaki, K. Sato, M. A. Haque, T. Nakajima and J. P. Gong, *Nat. Mater.*, 2013, **12**, 932–937.
8 J.-Y. Sun, X. Zhao, W. R. K. Illeperuma, O. Chaudhuri, K. H. Oh, D. J. Mooney, J. J. Vlassak and Z. Suo, *Nature*, 2012, **489**, 133–136.
9 Y. Wang, G. Nian, J. Kim and Z. Suo, *J. Mech. Phys. Solids*, 2023, **170**, 105099.
10 T. Nonoyama and J. P. Gong, *Annu. Rev. Chem. Biomol. Eng.*, 2021, **12**, 393–410.
11 J. P. Gong, Y. Katsuyama, T. Kurokawa and Y. Osada, *Adv. Mater.*, 2003, **15**, 1155–1158.
12 H. J. Zhang, T. L. Sun, A. K. Zhang, Y. Ikura, T. Nakajima, T. Nonoyama, T. Kurokawa, O. Ito, H. Ishitobi and J. P. Gong, *Adv. Mater.*, 2016, **28**, 4884–4890.
13 C. Imaoka, T. Nakajima, T. Indei, M. Iwata, W. Hong, A. Marcellan and J. P. Gong, *Sci. Adv.*, 2023, **9**, eabp8351.
14 C. Norioka, Y. Inamoto, C. Hajime, A. Kawamura and T. Miyata, *NPG Asia Mater.*, 2021, **13**, 34.
15 J. Kim, G. Zhang, M. Shi and Z. Suo, *Science*, 2021, **374**, 212–216.
16 G. Nian, J. Kim, X. Bao and Z. Suo, *Adv. Mater.*, 2022, **34**, 2206577.
17 D. Zhong, Z. Wang, J. Xu, J. Liu, R. Xiao, S. Qu and W. Yang, *Nat. Commun.*, 2024, **15**, 5896.
18 J. Ma, X. Zhang, D. Yin, Y. Cai, Z. Shen, Z. Sheng, J. Bai, S. Qu, S. Zhu and Z. Jia, *Adv. Mater.*, 2024, **36**, 2311795.
19 G. Zhang, J. Steck, J. Kim, C. H. Ahn and Z. Suo, *Sci. Adv.*, 2023, **9**, 1–8.
20 X. Hou, B. Huang, L. Zhou, S. Liu, J. Kong and C. He, *Adv. Mater.*, 2023, **35**, 2301532.
21 S. Lin, X. Liu, J. Liu, H. Yuk, H.-C. Loh, G. A. Parada, C. Settens, J. Song, A. Masic, G. H. McKinley and X. Zhao, *Sci. Adv.*, 2019, **5**, 1–9.
22 C. Yang, T. Yin and Z. Suo, *J. Mech. Phys. Solids*, 2019, **131**, 43–55.
23 X. Hou, W. Sun, Z. Liu, S. Liu, J. C. C. Yeo, X. Lu and C. He, *Macromolecules*, 2022, **55**, 5527–5534.
24 X. Hou, S. Sitthisang, B. Song, X. Xu, W. Jonhson, Y. Tan, S. Yodmuang and C. He, *ACS Appl. Mater. Interfaces*, 2024, **16**, 2912–2920.
25 X. Hou, Z. Zhu, Y. Wen, Y. Zhang, C. Thedrattanawong, D. Andreeva, J. Li and C. He, Melt Densification Enables Fracture-resistant Blend Hydrogels, 2025, preprint (version 1), DOI: 10.21203/rs.3.rs-6592950/v1.

26 X. Hou, S. Liu and C. He, *J. Mater. Chem. A*, 2022, **10**, 1497–1505.
27 J. C. C. Yeo, J. K. Muiruri, J. J. Koh, W. Thitsartarn, X. Zhang, J. Kong, T. T. Lin, Z. Li and C. He, *Adv. Funct. Mater.*, 2020, **30**, 1–12.
28 J. Kim, G. Zhang, M. Shi and Z. Suo, *Science*, 2021, **374**, 212–216.
29 W. Zhang, X. Liu, J. Wang, J. Tang, J. Hu, T. Lu and Z. Suo, *Eng. Fract. Mech.*, 2018, **187**, 74–93.
30 N. Rauner, M. Meuris, M. Zoric and J. C. Tiller, *Nature*, 2017, **543**, 407–410.
31 H. Tada, P. C. Paris and G. R. Irwin, *The Stress Analysis of Cracks Handbook*, ASME Press, 3rd edn, 2000, DOI: **10.1115/1.801535**.

